Performance of Satellite Rainfall Estimation Algorithms during TOGA COARE

ELIZABETH E. EBERT AND MICHAEL J. MANTON

Bureau of Meteorology Research Centre, Melbourne, Australia

(Manuscript received 6 February 1996, in final form 27 August 1996)

ABSTRACT

Over 50 satellite rainfall algorithms were evaluated for a 5° square region in the equatorial western Pacific Ocean during TOGA COARE, November 1992–February 1993. These satellite algorithms used GMS VIS/IR, AVHRR, and SSM/I data to estimate rainfall on both instantaneous and monthly timescales. Validation data came from two calibrated shipboard Doppler radars measuring rainfall every 10 min.

There was large variation among algorithms in the magnitude of the satellite-estimated rainfall, but the patterns of rainfall were similar among algorithm types. Compared to the radar observations, most of the satellite algorithms overestimated the amount of rain falling in the region, typically by about 30%. Patterns of monthly observed rainfall were well represented by the satellite algorithms, with correlation coefficients with the observations ranging from 0.86 to 0.90 for algorithms using geostationary data and 0.69 to 0.86 for AVHRR and SSM/I algorithms when validated on a 0.5° grid. Patterns of instantaneous rain rates were also well analyzed, with correlation coefficients with the radar observations of 0.43–0.58 for the geostationary algorithms and 0.60–0.78 for SSM/I algorithms.

Two case studies are presented to demonstrate the capability of one IR algorithm and three microwave algorithms to estimate instantaneous rainfall rates in the Tropics. The three microwave algorithms differed in their estimates of rain area but all showed greater ability than the IR algorithm to reproduce the spatial pattern of rainfall.

1. Introduction

Satellite remote sensing techniques have shown considerable promise for deriving estimates of rainfall on a global scale. Beginning in 1987 satellite rainfall estimates have been combined with surface observations to provide global monthly rainfall estimates for the Global Precipitation Climatology Project (GPCP) (Arkin and Xie 1994). Both NOAA and NASA Goddard Space Flight Center currently use microwave satellite observations to produce global monthly rainfall estimates that are available to the public through the Internet (Weng et al. 1994; Ferraro and Marks 1995; Adler et al. 1994). These rainfall estimates are being used in many applications such as climate diagnostics studies (e.g., Rasmussen and Arkin 1993), validation of rainfall forecasts from numerical weather prediction (NWP) models (e.g., Janowiak 1992), and as input for surface process models (Shinoda and Lukas 1995).

It is therefore of great interest to know: How accurate are these satellite rainfall estimates? How and why do estimates from different algorithms differ? Can satellite rainfall estimates be improved, and if so, how?

In order to address these issues, several algorithm intercomparison projects have been conducted. The WetNet Precipitation Intercomparison Projects, PIP-1 and PIP-2, examined the abilities of various algorithms that use passive microwave data from the Special Sensor Microwave/Imager (SSM/I) onboard the Defense Meteorological Satellite Program (DMSP) polar orbiting satellites. PIP-1 took the broad view, evaluating satellite estimates of monthly rainfall at coarse grid resolution (2.5°) over the globe (Barrett et al. 1994), while PIP-2 concentrated on pixel-scale estimates of instantaneous rain rates to try to pinpoint reasons for differences between algorithms (Smith et al. 1998).

The GPCP has conducted three algorithm intercomparison projects, AIP-1, AIP-2, and AIP-3 (Arkin and Xie 1994; Ebert et al. 1996). The strategy of the AIPs was to focus on a small region in space and time for which there were both abundant satellite visible/infrared and passive microwave data, and also very high quality surface validation data. AIP-1 evaluated the performance of satellite rainfall algorithms over Japan and surrounding waters during June–August 1989, while AIP-2 evaluated algorithms using data from western Europe during February–April 1991. AIP-3 evaluated satellite estimates of tropical convective rainfall in the equatorial Western Pacific during November 1992–February 1993, using as validation data the shipboard radar rainfall observations collected during the Tropical

Corresponding author address: Elizabeth E. Ebert, Bureau of Meteorology Research Centre, G.P.O. Box 1289 K, Melbourne, Victoria 3001, Australia.
E-mail: e.ebert@bom.gov.au

TABLE 1. Input and validation data used in AIP-3.

Data type	Platform	Resolution	Source
Satellite data			
Hourly geostationary visible and infrared (VIS/IR) imagery	GMS-4	5 km	JMA
AVHRR 5-channel VIS/IR imagery	NOAA-11, -12	1 km	U. Colorado
SSM/I 7-channel passive microwave imagery	DMSP F-10, F-11	25 km (ch. 1–5) 12.5 km (ch. 6–7)	NOAA
NWP data			
Daily analyzed 3-dimensional atmospheric fields (MSLP; Z, T, u, v, RH at 11 vertical levels)	ECMWF T213 spectral model	~0.52°	ECMWF
Daily precipitation forecasts (12–36 h forecast)	ECMWF T213 spectral model	~0.52°	ECMWF
Daily precipitation forecasts (sum of 6-h forecasts)	NMC medium-range model	2.5°	NMC
6-hourly precipitation forecasts	JMA T106L21 spectral model	~225°	JMA
Ancillary data			
Climatological monthly rainfall from Pacific atolls	Rain gauges	Point measurements	Morrissey and Greene (1991)
GCM monthly rainfall estimates	Max-Planck Institute GCM	2.82°	K. Arpe
Validation data			
Radar rain rates every 10 min	MIT, TOGA shipboard radars	2 km	NASA GSFC

GMS: Geostationary Meteorological Satellite
AVHRR: Advanced Very High Resolution Radiometer
SSM/I: Special Sensor Microwave/Imager
DMSP: Defense Meteorological Satellite Program
NMC: National Meteorological Center
NASA: National Aeronautics and Space Administration
JMA: Japan Meteorological Agency
NOAA: National Oceanic and Atmospheric Administration
ECMWF: European Centre for Medium-Range Weather Forecasts
GSFC: Goddard Space Flight Center

Ocean Global Atmosphere Coupled Ocean–Atmosphere Response Experiment (TOGA COARE).

This paper presents some of the findings of AIP-3. Section 2 details the data used in the experiment, and section 3 gives an overview of the algorithms that were evaluated. The main results of AIP-3 are presented in section 4. Section 5 examines the performance of four widely available algorithms for two case studies. Finally, some conclusions are given in section 6. A complete compilation of the results of AIP-3 can be found in Ebert (1996).

2. Data

a. Input data

The input dataset for AIP-3, detailed in Table 1, contained satellite, NWP, and ancillary data in a 5° square region in the western Pacific (1°N–4°S, 153°–158°E) during the months of TOGA COARE, November 1992 through February 1993. The satellite input data included hourly Geostationary Meteorological Satellite (GMS) visible/infrared imagery, 5-channel Advanced Very High Resolution Radiometer (AVHRR) visible/infrared imagery, and SSM/I passive microwave data. Daily numerical weather prediction analyses and model output from ECMWF, JMA, and NMC (renamed NCEP) were provided for use in those algorithms that require additional information about the atmospheric state. Monthly GCM rainfall estimates for the TOGA COARE period were provided by the Max Planck Institute. Monthly Pacific atoll rain gauge measurements from 20 years predating the TOGA COARE period (Morrissey and Greene 1991) were also provided.

b. Validation data

Validation data consisted of maps of calibrated radar rain rates collected from two shipboard Doppler radars (MIT and NOAA/TOGA) located at approximately 2°S, 154.5°E and 2°S, 156°E, as shown in Fig. 1 (Short et al. 1997). The maximum usable range of each radar was 145 km, yielding rainfall measurements in a circular

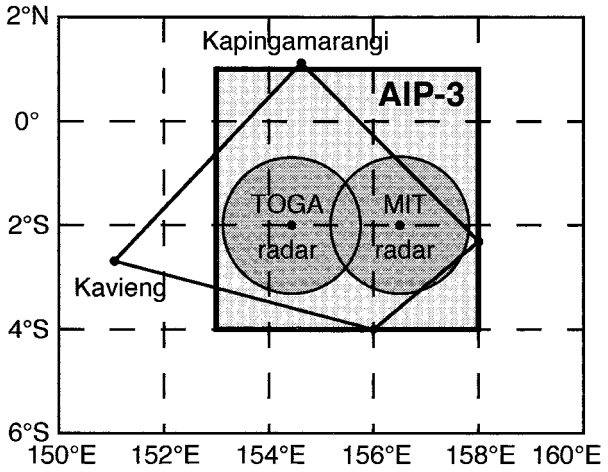

FIG. 1. Region of the TOGA COARE Intensive Flux Array showing the AIP-3 region and positions of the radar ships.

region approximately 2.5° in diameter. In the regions of overlap of the two radar ranges the maximum of the two rainfall rates was retained for each pixel. With both radars deployed, about one-third of the AIP-3 5° square region contained radar rainfall measurements.

The calibration of the radars is discussed in detail in Short et al. (1997). Briefly, radar reflectivities were measured every 10 min at a scan height of 2 km. In order to reduce the effects of random error, a Cartesian subresolution sampling scheme was used to average 8×8 arrays of raw data onto a 2-km grid. The radar reflectivities were converted to rainfall rates using a *Z–R* relationship of

$$Z = 120R^{1.43} \tag{1}$$

for convective rain. Point estimates of rainfall measured by optical rain gauges on moorings and ships during TOGA COARE were not considered accurate enough to be used in the validation process or to calibrate the shipboard radars. Therefore, the *Z–R* relation was derived by calibrating the radar measurements against disdrometer data from Kapingamarangi Atoll.

Initially a *Z–R* relation of $Z = 139R^{1.43}$ was used for convective rainfall (''version 1''). The version 1 rainmaps were used to produce an initial set of AIP-3 satellite algorithm validation statistics. These statistics revealed that the radar rain rates were significantly lower than all but one of the satellite and NWP estimates, typically by a factor of 0.5–0.7, suggesting a likely systematic bias. Further examination of the range dependence of the radar rain rates led to an increase in the attenuation coefficient. Recent studies using profiling radars in TOGA COARE showed that the vertical fall speed of raindrops decreased by about 10% between 2-km altitude and the surface, which led to a revision of the *Z–R* relation. The combined effect of these improvements in calibration (''version 2'') was to increase the radar rain rates by an average of about 30% (Ferrier et al.)

These version 2 radar rain rates were treated as ''truth'' against which to compare the satellite algorithms. In the strictest sense, AIP-3 was really an intercomparison between remote sensing estimates, with the radar given greater credibility. It is believed that the radar reliably detected the presence or absence of rain, but the residual uncertainty in calibration must lead to uncertainties in satellite algorithm bias and other validation statistics. Thus, we will use the word ''intercomparison'' in preference to ''validation'' throughout this paper.

Convective/stratiform maps were also produced to identify the different rain regimes using a modified Houze technique (Churchill and Houze 1984). Results from previous studies suggested that, for the same radar reflectivity, stratiform rain rates should be approximately half the magnitude of convective rain rates. The *Z–R* relationship adopted for stratiform rain was

$$Z = 323R^{1.43}. \tag{2}$$

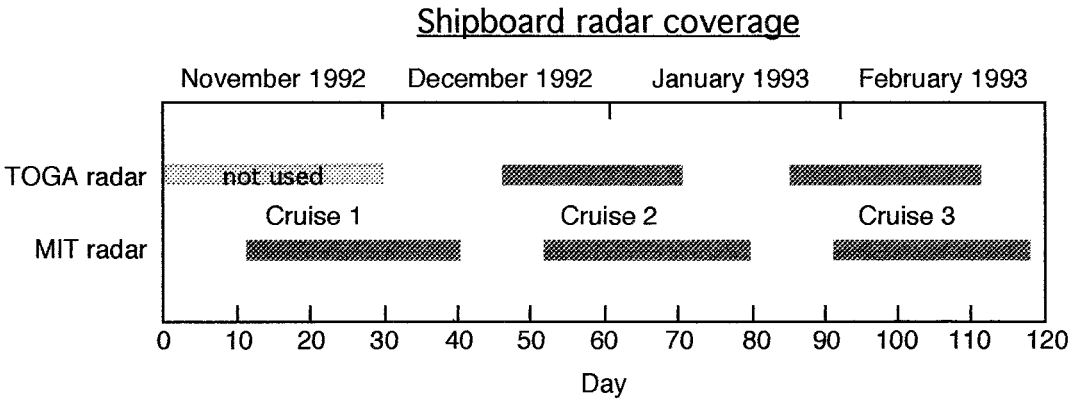

FIG. 2. Deployment of shipboard Doppler radars during TOGA COARE. Rain rates from the TOGA radar during Cruise 1 were not used due to large uncertainties in the radar calibration.

TABLE 2. Summary of algorithms submitted to AIP-3.

Code	Algorithm (reference)	Data	Rain detection	Rain-rate (RR) estimation	Calibration/training
IR algorithms					
AD5	NAWT (based on Negri et al. 1984)	IR	$T_B \leq 235$ K	10%, 50% T_B thresholds applied to cloud entities	Florida (orig.), then GSCAT RRs from TOGA COARE
AD6	CST (based on Adler and Negri 1988)	IR	$T_B \leq 235$ K	RR a function of T_B distribution within cloud entities	Florida (orig.), then GSCAT RRs from TOGA COARE
AR1	GPI (Arkin and Meisner 1987)	IR	$T_B \leq 235$ K	RR = const	GATE
AR2	Modified GPI		$T_B \leq 235$ K		GATE
AR3	Modified GPI		$T_B \leq 225$ K		GATE
GA1	IR technique (Grassotti and Garand 1994)	IR, T profile	Cloud classification	Class-dependent RR	GMS IR–AMeDAS matchups from Japan (AIP-1)
JO1	RACC (Jobard and Desbois 1994)	IR	Pixel classification	Class-dependent RR	Dynamic clustering of METEOSAT IR–$RR_{\mu w}$ matchups from West Africa
KR1	IR technique (submitted by T. Kurino)	IR in consecutive images	—	Lookup tables based on T_B, temporal variation, spatial properties	GMS IR–AMeDAS matchups from Okinawa
MA1	μwave-trained IR (submitted by D. Martin and B. Hinton)	IR	T_B threshold	RR a polynomial function of T_B	GMS IR–$RR_{\mu w}$ matchups from TOGA COARE (Cal/Val), probability matching
MA3	IPR (Goodman et al. 1993)	IR	$T_B \leq 253$ K	RR an exponential function of T_B	GOES IR–rain gauge matchups from Amazon Basin
MA2	Modified IPR			As above, with cold temperature cutoff	
MA4	Hybrid algorithm (submitted by D. Martin and B. Hinton)	IR	T_B threshold	RR is average of MA1 and MA3	
MO1	Modified GPI (submitted by M. Morrissey)	IR	$T_B \leq 235$ K	Slope, intercept applied to GPI RR	Pacific atoll rain gauges
VIS/IR algorithms					
GA2	VIS/IR technique (Grassotti and Garand 1994)	VIS, IR, T profile	Cloud classification	Class-dependent RR	GMS IR–AMeDAS matchups from Japan (AIP-1)
HO1	RAINSAT (Hogg 1990)	VIS, IR	Classification of pixels in 2D histogram	Class-dependent RR	GOES VIS/IR–radar matchups from southern Ontario
KR2	VIS/IR technique (submitted by Y. Yotsuya and T. Kurino)	VIS, IR	Threshold on thick cloud ratio	Lookup tables based on T_B and thick cloud ratio	GMS VIS/IR–AMeDAS matchups from Okinawa
AVHRR algorithm					
IN1	Split window (submitted by T. Inoue)	AVHRR ch. 4,5	T_4–T_5 threshold	RR an exponential function of T_B	GMS IR–*Keifu-maru* radar matchups in TOGA COARE
Mixed IR/SSM/I algorithms					
AD2 KM2	IR area-matching (submitted by R. Adler and C. Kummerow)	IR, 37H, 85H IR, all SSM/I ch	Monthly varying T_B threshold	Monthly varying conditional rain rate	Probability matching using GMS IR–$RR_{\mu w}$ matchups from TOGA COARE (AD1 and KM1)
AD3 KM3	Adjusted GPI (Adler et al. 1993) (monthly only)	IR, 37H, 85H IR, all SSM/I ch	—	Monthly varying multiplying factor for GPI	GMS IR–$RR_{\mu w}$ matchups from TOGA COARE (AD1 and KM1)
AD4 KM4	IR rain volume matching (submitted by R. Adler and C. Kummerow)	IR, 37H, 85H IR, all SSM/I ch	Monthly varying T_B threshold	Monthly varying NAWT T_B thresholds	Probability matching using GMS IR–$RR_{\mu w}$ matchups from TOGA COARE (AD1 and KM1)

TABLE 2. (*Continued*).

Code	Algorithm (reference)	Data	Rain detection	Rain-rate (RR) estimation	Calibration/training
BE2	(Berg 1994)	IR, 19H, 22V, 37V, 37H	—	RR a function of IR T_B class	Probability matching using GMS IR–$RR_{\mu w}$ matchups from TOGA COARE (BE1 and FR1)
BE3		IR, all SSM/I ch	—		
SH1	SSM/I–ISCCP algorithm (Liu et al. 1995)	ISCCP T_c, τ_{vis}, 19H, 37H, 37V, 85H	—	Lookup tables based on T_c and τ_{vis}	ISCCP–$RR_{\mu w}$ matchups from TOGA COARE (LI1)
SSM/I algorithms					
AD1	GSCAT-2 (Adler et al. 1993)	37H, 85H	Multispectral screen for nonraining pixels	RR a linear function of T_B(85H)	RT calculations, adjusted using Pacific atoll rain gauge data
AO1	(Aonashi et al. 1996)	19V, 37V, 85H, T and q profiles	—	Inversion to derive rain rate	RT calculations using cloud and atmospheric profiles
BA0	Modified Cal/Val. (submitted by C. Kidd and E. Barrett)	19H, 22V, 37V, 37H	Latitude-dependent thresholds on T_B(19H) and T_B(37V)–T_B(37H)	RR a linear function of T_B's	Cal/Val · 2, as suggested by PIP-1
BA1	HFVFD (submitted by C. Kidd and E. Barrett)	37V, 85V	—	RR a quadratic function of HFVFD = a · T_B(37V) − T_B(85V)-b	FRONTIERS radar data over British Isles
BA2	PCT (submitted by C. Kidd and E. Barrett)	85V, 85H	Screen out snow pixels after Fiore and Grody (1990)	RR a quadratic function of PCT = (1 + t) · T_B(85V) − t · T_B(85H)	FRONTIERS radar data over British Isles
BA3	LFVFD (submitted by C. Kidd and E. Barrett)	19V, 85V	—	RR a quadratic function of LFVFD = a · T_B(19V) − T_B(85V)-b	FRONTIERS radar data over British Isles
BA4	Scattering index (submitted by D. Smith and E. Barrett)	37V, 37H, 85V, 85H	Scattering index threshold	Lookup table based on T_B(37V)–T_B(37H), scattering RR is linear function of T_B(85V) and T_B(85H)	FRONTIERS radar data over British Isles
BA5	(submitted by D. Smith and E. Barrett)	37V, 85V, 85H	Threshold outside 2 std. devs. on T_B(85H) vs T_B(85V) plot	RR a linear function of T_B's	FRONTIERS radar data over British Isles
BE1	Modified Cal/Val (Berg and Chase 1992)	19H, 22V, 37V, 37H	Latitude-dependent thresholds on T_B(19H) and T_B(37V)–T_B(37H)	RR a linear function of T_B's	Rain gauge data
CH1	(based on Wilheit et al. 1991)	19V, 22V	Low rain-rate cutoff	Iterative retrieval of freezing level, then RR a function of T_B's at 19, 22, 85 GHz	RT calculations using cloud model
FE1	Scattering algorithm (Ferraro and Marks 1995) (FE1 and FE4 have slightly different coefficients)	19V, 22V, 85V	Scattering index SI ≥ 10 for rain	RR an exponential function of SI = a + b · T_B(19V) + c · T_B(22V) + d · T_B(22V)² − T_B(85V)	Radar data from Japan, UK, USA
FE4					
FE2	Emission algorithms (Ferraro and Marks 1995)	19V, 22V, 37V	Liquid water Q > threshold	RR an exponential function of Q estimated using 19V (FE2) or 37V (FE3)	Radar data from Japan, UK, USA
FE3					
FR1	Physical algorithm (Ferriday and Avery 1994)	19V, 19H, 22V, 37V, 37H, 85H	T_B thresholds	RR a linear function of T_B's	RT calculations using cloud model
HA1	(submitted by T. Hayasaka and Takizawa)	All SSM/I ch.	Rain mask using T_B(37V)–T_B(37H)	85 GHz → stratiform or convective, then RR a linear function of T_B's	RT calculations using tropical atmosphere and cloud model
IA1	(submitted by J. Haferman and W. Krajewski)	All SSM/I ch.		RR a logarithmic function of T_B(22V)–T_B(19H)	RT calculations using stochastic rainfall model
IA2	(submitted by J. Haferman and W. Krajewski)	All SSM/I ch.		Neural network classification of T_Bs	RT calculations using stochastic rainfall model

TABLE 2. (*Continued*).

Code	Algorithm (reference)	Data	Rain detection	Rain-rate (RR) estimation	Calibration/training
IA3	(Morrissey et al. 1994) (monthly only)	Results from any algorithm	—	RR (mm/mon) = 2932.2 F + 276.075, F = fraction of month that rain fell anywhere in 0.5° box	
KM1	Physical retrieval (Kummerow and Giglio 1994)	All SSM/I ch.	Rain mask using T_B(37V)–T_B(37H)	Iterative retrieval of cloud structure → rain rate	RT calculations using multiple rain structures
LI1	Physical algorithm (Liu and Curry 1992)	19H, 37H, 37V, 85H	Thresholds of T_B(19H), T_B(37H), T_B(37V), T_B(85H)	RR an exponential function of [T_B(19H)–T_B(85H)]	RT calculations using cloud model
MZ1	Maximum likelihood retrieval (Marzano et al. 1995)	19V, 19H, 37V, 37H, 85V, 85H	Rain mask using T_B(85V)–T_B(85H)	Maximum likelihood classifiation of cloud structure	RT calculations using mesoscale cloud model
MZ2	Multiple regression retrieval (Basili et al. 1995)	19V, 19H, 37V, 37H, 85V, 85H		Discriminant analysis classification of cloud structure	
PE1	Physical inversion (Petty and Stettner 1994)	19V, 19H, 37V, 37H, 85V, 85H	Rain mask using T_B(85V)–T_B(85H)	Polarization-based inversion of cloud properties → rain rate	RT calculations using cloud model
PE2	Scattering algorithm (submitted by G. Petty)	85V, 85H	Rain mask using T_B(85V)–T_B(85H)	Scattering-based first guess using 85-GHz polarization	RT calculations using cloud model
PR1	(submitted by C. Prabhakara)	19V, 19H, 37V, 37H, 85V, 85H	Threshold on T_B(37H)	RR = C · [T_B(85H)–T_B(37H)]/[275 − T_B(19H)]	RT calculations using cloud model
SC1	(Bauer and Schlüssel 1993)	19V, 19H, 22V, 37H, 85V, 85H	RR < 0.3 mm h^{-1} or Q < 0.1 g cm^{-2} → nonraining	Logarithm of RR is a polynomial function of T_B's	RT calculations using cloud model
SM1	FSU profile algorithm (Smith et al. 1994)	19V, 19H, 37V, 37H, 85V, 85H	Similiar to Grody (1991) scheme	Iterative retrieval of cloud structure → rain rate	RT calculations using mesoscale cloud model
SM2	High resolution version				
WI1	Emission algorithm (Wilheit et al. 1991)	19V, 19H, 22V, 37V, 37H	Low rain-rate cutoff	Iterative retrieval of freezing level, then RR = max[RR(19GHz), RR(37GHz)]	RT calculations using physical cloud model

c. Gridding and treatment of missing data

A spatial grid scale of 0.5° was used in the intercomparison. This resolution was chosen so that each sample would represent a fairly large area, as in the GPCP product, while also providing enough samples to enable meaningful intercomparison statistics to be computed.

The radar data were mapped onto the validation grid in the following manner. First, an effort was made to replace any missing 2-km resolution pixels with the average of the four nearest neighbors in space. If all of those were also missing, then the pixel was replaced by the rainfall rate from the previous time step (generally 10 min prior, but no more than 30 min). If that was missing as well, then no further action was taken. The 2-km radar pixels were then averaged onto the 0.5° grid, with a grid value being considered valid only if at least 80% of the pixels contained good (original) data. This requirement eliminates most of the rain rates from the periphery of the radar scans (which are those most likely to be influenced by attenuation effects and are therefore less reliable).

Monthly gridded radar rainfall was obtained in a similar manner. TOGA COARE cruise ''months'' were used to evaluate the algorithms on monthly timescales (Fig. 2). A cruise ''month'' was defined as a block of consecutive, complete days during which at least one shipboard radar was located completely inside the 5° square AIP-3 region. These were:

Month 1 ≡ Cruise 1: 11 November–10 December 1992;
Month 2 ≡ Cruise 2: 15 December 1992–18 January 1993;
Month 3 ≡ Cruise 3: 23 January–23 February 1993.

The number of days in each cruise was 30, 35, and 32 days, respectively. The monthly totals were created in the following manner. All available radar rain estimates were summed to get daily totals at the full 2-km spatial resolution, with a daily sum being considered valid for a pixel if good data were recorded at least 80% of the time during the day. Each pixel was scaled appropriately to represent the total daily rainfall [i.e., an average rain rate was computed (mm h^{-1}), then multiplied by 24 h]. The daily values were summed and scaled appropriately for the ''month'' with the requirement that at least 80% of daily values be present during the ''month.'' The monthly totals were then averaged in space to produce the 10 × 10 gridded values. As with the instantaneous grids, each monthly grid box was required to contain at least 80% good (original) data in order to be considered valid. After spatial averaging to the 0.5° grid each ''month'' contained between 10 and 16 pairs of matched estimates and observations.

3. Algorithms

The satellite rainfall algorithms evaluated in AIP-3 fell into five categories. Infrared (IR) algorithms relate the rainfall rate to the cloud brightness temperature T_B, implicitly assuming that deeper, colder clouds are more likely to produce heavy rainfall (e.g., Richards and Arkin 1981). Some IR algorithms augment the infrared imagery with visible imagery (VIS/IR), using the cloud albedo to indicate optically thick clouds that may be precipitating (e.g., Hogg 1990). AVHRR algorithms use the infrared split window to detect thin cirrus (Inoue 1987) or to sense water droplet size at cloud top (Rosenfeld and Gutman 1994). SSM/I algorithms can sense the emission of microwave radiation from liquid precipitation particles using the lower-frequency channels (19, 22, 37 GHz), as well as scattering of high-frequency (85 GHz) microwave radiation from frozen precipitation particles (e.g., Grody 1991). Finally, a new class of algorithms is emerging that uses the SSM/I algorithms to ''calibrate'' the IR algorithms on a monthly basis (''mixed'' IR–SSM/I), thus taking advantage of both the superior spatial and temporal sampling provided by the geostationary satellites and the more physically based (and presumably more accurate) nature of the SSM/I algorithms.

A total of 57 satellite rainfall algorithms were submitted by 24 research groups. Each algorithm was assigned a three-character code name indicating the investigator and the version number of the algorithm within the set of results submitted by the group (for example, AD5 refers to the fifth algorithm submitted by Adler's group). Table 2 lists the algorithms that were evaluated in AIP-3, along with an abbreviated summary of their methodologies. Short descriptions of the algorithms may be found in Ebert (1996); for full descriptions of the algorithms the reader should consult the original references cited in column 2 of the table.

There were more algorithms evaluated in AIP-3 than in AIP-1 and AIP-2 combined. This is mainly a result of the rapid growth in the number of SSM/I rainfall algorithms, as well as a recent effort by many algorithm developers to combine IR and microwave data into mixed algorithms. Rainfall algorithms were permitted to use any combination of satellite, NWP, and ancillary data. In addition, the NWP precipitation forecasts were also validated to assess the relative merits of satellite-observed versus model-forecast rainfall.

AIP-3 participants provided rainfall estimates for every GMS image, AVHRR image, or SSM/I swath (depending on the algorithm) in the AIP-3 dataset. Rainfall estimates using GMS data were produced on a 0.5° latitude–longitude (10 × 10) grid (i.e., the validation grid), AVHRR estimates on a 0.1° (50 × 50) grid, and SSM/I estimates at full pixel resolution (12.5 or 25 km). Area-weighted averaging was used to map the AVHRR and SSM/I estimates onto the validation grid, while bilinear interpolation was used to obtain 0.5° gridded rainfall estimates from the NWP forecasts. In addition, (calendar) monthly estimates on a 0.5° grid were produced by all groups.

Cruise monthly rainfall estimates were produced for

TABLE 3. Rain/no rain contingency table.

		Estimated	
		No rain	Rain
Observed	no rain	a	b
	rain	c	d

all algorithms for each of the three TOGA COARE cruises. Missing pixels in the geostationary analyses were replaced by the average of the nearest estimates in time, then simply summed for the cruise to get monthly estimates. For AVHRR and SSM/I rainfall estimates average rain rates for each grid box were calculated and multiplied by the number of hours in the cruise to obtain monthly estimates. No attempt was made to replace missing data in the AVHRR and SSM/I analyses or to account for possible diurnal bias. Monthly NWP rainfall estimates were obtained by summing the daily values. In addition, a ''climatology'' estimate was generated from the 20-year set of monthly Pacific atoll rainfall observations by analyzing them onto a grid using a Barnes analysis, then interpolating to obtain values for the appropriate cruise dates.

4. Overall results of AIP-3

Three timescales were considered: instantaneous, daily, and monthly; this paper reports the intercomparison results for instantaneous and monthly rainfall. The statistical analysis was similar to those carried out in AIP-1 and AIP-2 (Lee et al. 1991; Allam et al. 1993). A large number of intercomparison statistics were computed, not all of which are tabulated in this paper. The results shown here include the number of data points, mean radar-estimated and satellite-estimated rainfall, bias (the difference between the mean satellite and mean radar rainfall), ratio of the estimated to observed rainfall, root-mean-square difference, bias-adjusted rms difference (the rms difference obtained when the bias is subtracted from the set of estimates, giving the error standard deviation), and the correlation coefficient between satellite and radar rainfall. For the instantaneous rain rates three statistics were computed from the rain/no rain contingency table (shown in Table 3): the probability of detection, POD, measures the fraction of grid boxes with radar-observed rain for which rain was also predicted:

$$\mathrm{POD} = d/(c + d); \tag{3}$$

the false alarm ratio, FAR, gives the fraction of rain predictions that were actually nonraining:

$$\mathrm{FAR} = b/(b + d); \tag{4}$$

and the 2 × 2 skill, which is the number of correct diagnoses divided by the expected number correct due to chance:

$$\mathrm{skill} = (a + d - E)/(a + b + c + d - E), \tag{5}$$

where

$$E = [(a + b)(a + c) + (c + d)(b + d)] \div (a + b + c + d).$$

A threshold of 0.025 mm h^{-1} was applied to the radar and satellite rainfall estimates to delineate ''rain'' and ''no rain.'' The rationale for this threshold is that rain rates below 0.1 mm h^{-1} are virtually impossible to detect in SSM/I imagery; 0.025 mm h^{-1} represents one-quarter of this value, since approximately four (25 km) SSM/I pixels cover the same area as a 0.5° grid box.

In the analysis to follow, the term ''IR-based algorithms'' is used to denote the set of IR, VIS/IR, AVHRR, and mixed IR–SSM/I algorithms. Results from five algorithms were excluded from this report; IR algorithms MA1, MA2, MA3, and MA4 were found to have incorrect dates and times for many of the analyses, and estimates from SSM/I algorithm MZ2 were produced for only a small number of swaths. Mixed algorithm SH1 used International Satellite Cloud Climatology Project (ISCCP) estimates of cloud optical depth as input data, and as a result gave 3-h rain rate estimates instead of hourly. Algorithm HA1 provided estimates from only one DMSP satellite, resulting in only half as many samples as the other SSM/I algorithms. Algorithm IA3 provided estimates for calendar months, but it was not possible to convert these estimates to cruise months.

a. Monthly rainfall

The algorithms' performance on a monthly timescale is of particular importance to the GPCP. Table 4 lists the intercomparison statistics for estimated monthly rainfall using all satellite algorithms and NWP models, where all monthly estimates were pooled in space and time. The mean radar and satellite-estimated values refer to the average monthly rainfall across the three cruise ''months.''

It is evident from Table 4 that most of the satellite algorithms overestimated monthly rainfall relative to the radar observations. A few algorithms overestimated rain by a factor of 4–6, while a few estimated as little as two-thirds of the radar rainfall. The median value of the ratio was 1.3; that is, the satellite algorithms typically overestimated the monthly rainfall by about 30%.

The ratio of satellite to radar rainfall was not consistent over the entire period. Figure 3a shows a plot of the median monthly rainfall estimated by IR-based algorithms for each grid box versus the radar-estimated values; Fig. 3b shows a similar plot for SSM/I algorithms. In these plots each of the cruise ''months'' is indicated by a different symbol. Similar behavior is seen for both IR-based and SSM/I algorithms, except for Cruise 1, in which the SSM/I algorithms were more likely than IR-based algorithms to underestimate the rainfall derived from the radar. The greatest overesti-

TABLE 4. Intercomparison statistics for monthly rainfall for the three cruises combined.

Algorithm	Number of points	Mean radar (mm)	Mean satellite (mm)	Bias (mm)	Ratio	Rms diff. (mm)	Adj. rms diff. (mm)	Correlation coefficient
IR algorithms								
AD5	41	156.6	198.2	41.6	1.27	76.6	64.2	0.86
AD6	41	156.6	214.6	58.0	1.37	75.5	48.3	0.90
AR1	41	156.6	316.2	159.6	2.02	187.0	97.5	0.88
AR2	41	156.6	210.8	54.2	1.35	75.2	52.2	0.88
AR3	41	156.6	181.5	24.9	1.16	59.1	53.6	0.88
GA1	41	156.6	363.0	206.4	2.32	241.1	124.6	0.88
JO1	41	156.6	194.8	38.2	1.24	128.6	122.8	0.87
KR1	41	156.6	618.1	461.5	3.95	510.6	218.4	0.90
MO1	41	156.6	243.0	86.4	1.55	104.6	58.9	0.88
VIS/IR algorithms								
GA2	41	156.6	334.6	178.0	2.14	214.2	119.0	0.88
HO1	41	156.6	114.0	−42.6	0.73	54.2	33.6	0.87
KR2	41	156.6	365.5	208.9	2.33	239.6	117.4	0.87
AVHRR algorithms								
IN1	41	156.6	206.8	50.2	1.32	90.3	75.1	0.79
Mixed IR-SSM/I algorithms								
AD2	41	156.6	205.8	49.2	1.31	118.9	108.2	0.87
AD4	41	156.6	199.3	42.7	1.27	106.4	97.4	0.87
BE2	41	156.6	186.6	30.0	1.19	68.5	61.6	0.88
BE3	41	156.6	281.6	125.0	1.80	184.8	136.1	0.86
KM2	41	156.6	203.3	46.7	1.30	93.4	80.9	0.87
KM4	41	156.6	184.1	27.5	1.18	95.7	91.7	0.87
SH1	41	156.6	188.9	32.3	1.21	62.9	54.0	0.88
SSM/I algorithms								
AD1	41	156.6	202.8	46.2	1.30	159.1	152.2	0.78
AO1	41	156.6	144.0	−12.6	0.92	77.5	76.5	0.82
AO2	41	156.6	98.1	−58.5	0.63	88.4	66.3	0.78
BA0	41	156.6	259.4	102.8	1.66	153.0	113.3	0.85
BA1	41	156.6	169.8	13.2	1.08	82.9	81.8	0.85
BA2	41	156.6	214.6	58.0	1.37	113.2	97.3	0.86
BA3	41	156.6	302.2	145.6	1.93	203.9	142.7	0.86
BA4	41	156.6	326.9	170.3	2.09	218.9	137.5	0.85
BA5	41	156.6	530.9	374.3	3.39	503.4	336.6	0.83
BE1	41	156.6	172.0	15.4	1.10	74.0	72.4	0.80
CH1	41	156.6	162.8	6.2	1.04	69.4	69.2	0.81
FE1	41	156.6	185.9	29.3	1.19	130.0	126.7	0.79
FE2	41	156.6	243.8	87.2	1.56	201.1	181.2	0.71
FE3	41	156.6	205.8	49.2	1.31	119.2	108.5	0.83
FE4	41	156.6	190.7	34.1	1.22	124.3	119.6	0.80
FR1	41	156.6	310.2	153.6	1.98	209.3	142.2	0.79
HA1	41	156.6	193.8	37.2	1.24	171.2	167.1	0.69
IA1	41	156.6	789.4	632.8	5.04	764.5	428.9	0.83
IA2	41	156.6	776.8	620.2	4.96	749.7	421.2	0.85
KM1	41	156.6	165.2	8.6	1.05	105.5	105.1	0.72
LI1	41	156.6	108.7	−47.9	0.69	79.9	64.0	0.81
MZ1	41	156.6	231.8	75.2	1.48	160.6	141.9	0.82
PE1	41	156.6	196.3	39.7	1.25	125.6	119.2	0.79
PE2	41	156.6	222.0	65.4	1.42	139.9	123.7	0.84
PR1	41	156.6	258.9	102.3	1.65	193.9	164.7	084
SC1	41	156.6	154.0	−2.6	0.98	76.6	76.6	0.76
SM1	41	156.6	188.1	31.5	1.20	82.7	76.4	0.81
SM2	41	156.6	131.2	−25.4	0.84	67.7	62.8	0.75
WI1	41	156.6	158.7	2.1	1.01	85.0	85.0	0.80
NWP models								
ECM	41	156.6	323.7	167.1	2.07	201.5	112.5	0.39
JMA	41	156.6	610.7	454.1	3.90	550.6	311.3	0.37
NMC	41	156.6	273.9	117.3	1.75	140.7	77.8	0.38
Climatology								
CLI	41	156.6	244.4	87.8	1.56	110.8	67.5	−0.03

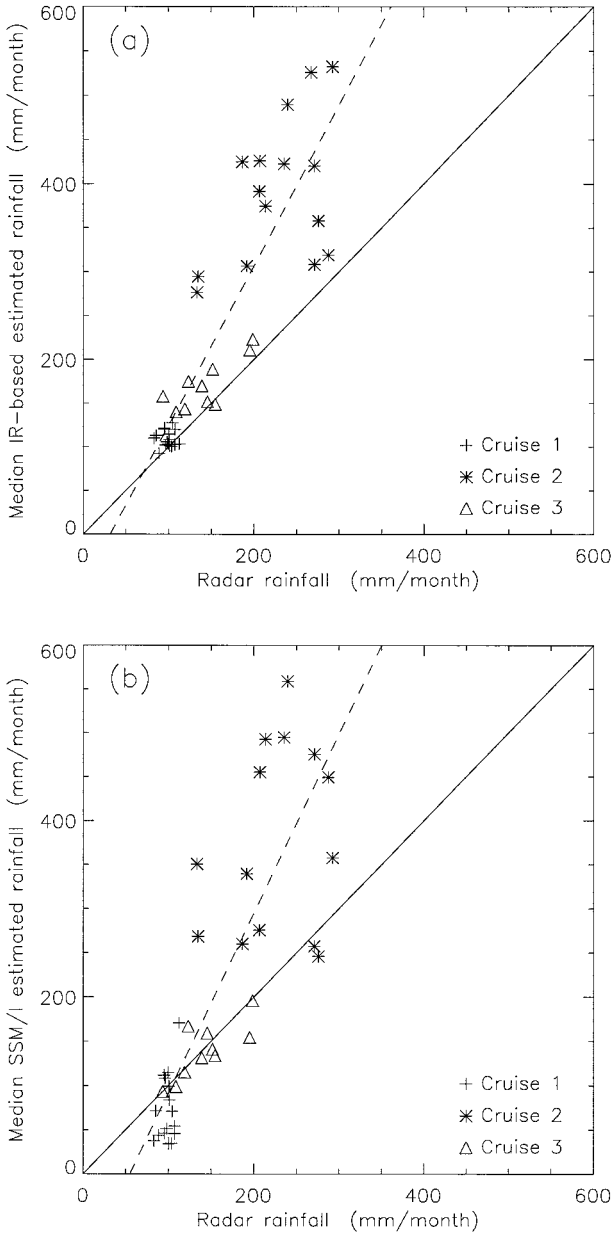

FIG. 3. Median satellite-estimated rainfall for each pixel and month versus the radar-estimated values for (a) IR-based algorithms and (b) SSM/I algorithms. Cruise 1 values are indicated by crosses, Cruise 2 values by asterisks, and Cruise 3 by open triangles.

mates occurred for Cruise 2, which was a period of enhanced convective activity in the TOGA COARE region (McBride et al. 1995). Median values of the ratio statistic for all algorithms were 0.75 for Cruise 1, which was a relatively quiet period, 1.7 for Cruise 2, and 1.4 for the third cruise.

It is interesting to note that the tendency for some satellite algorithms to underestimate the lower rainfall amounts and overestimate the higher rainfall amounts in AIP-3 is counter to the behavior of similar algorithms estimating monthly rainfall in AIP-1 and AIP-2 (Lee et al. 1991; Allam et al. 1993). This may have to do with the nature of the rainfall in TOGA COARE. Light rain periods were characterized by frequent shallow convection with cells that were too small to be resolved by the SSM/I algorithms and too warm to be detected by the IR-based algorithms. Periods of intense convection, such as occurred during Cruise 2, were accompanied by large cirrus shields that were misdiagnosed as raining by the IR-based algorithms. The reason for the SSM/I algorithms overestimating convective rainfall is unclear.

The rms differences ranged from about 50 to over 700 mm mo^{-1}, with the lowest values corresponding to those algorithms having the lowest bias values, and the largest rms differences corresponding to the highly biased algorithms. The bias-adjusted rms measures the standard deviation of the difference and was less than the magnitude of the mean radar-estimated rainfall for most of the algorithms. One VIS/IR algorithm, HO1 (RAINSAT), had an adjusted rms value of 21% of the radar-estimated monthly rain. The bias and adjusted rms difference of the ''climatology'' estimate were also lower than those of many of the satellite algorithms.

The correlation coefficient measures the ability of algorithms to detect changes in rainfall over space and time. There is a high degree of correlation between the satellite-estimated and radar-estimated monthly rainfall when all monthly estimates are considered together, with correlation coefficients ranging from 0.69 to 0.90. The NWP models were somewhat less skillful in estimating monthly precipitation, with correlation coefficients of around 0.4.

To determine whether these correlation coefficients were statistically significant and distinguishable from each other, an analysis of the correlation coefficients was carried out following Xie and Arkin (1995). They outline a pair of significance tests that take into account the nonrandom nature of the samples. An effective sample size is proposed that modulates the raw sample size using the spatial autocorrelation function. For the 41 monthly rainfall samples, the effective sample size ranged between 25 and 30, depending on the algorithm. The significance tests showed that all of the correlation coefficients were significantly different from zero, but that two given correlation coefficients must be separated by about 0.15–0.25 (for the range of correlations shown in Table 4) to be considered statistically different at the 95% confidence level. This indicates that it is not possible, from this limited number of samples, to determine with certainty which algorithm estimated monthly rainfall with the greatest skill. It is clear, however, that the satellite rainfall algorithms outperformed all of the NWP models and climatology.

Figure 4 shows a plot of the correlation coefficient between satellite-estimated and radar-estimated monthly rainfall versus the bias-adjusted rms difference normalized by the mean radar rainfall. Successful algorithms, that is, those with high correlations and low rms

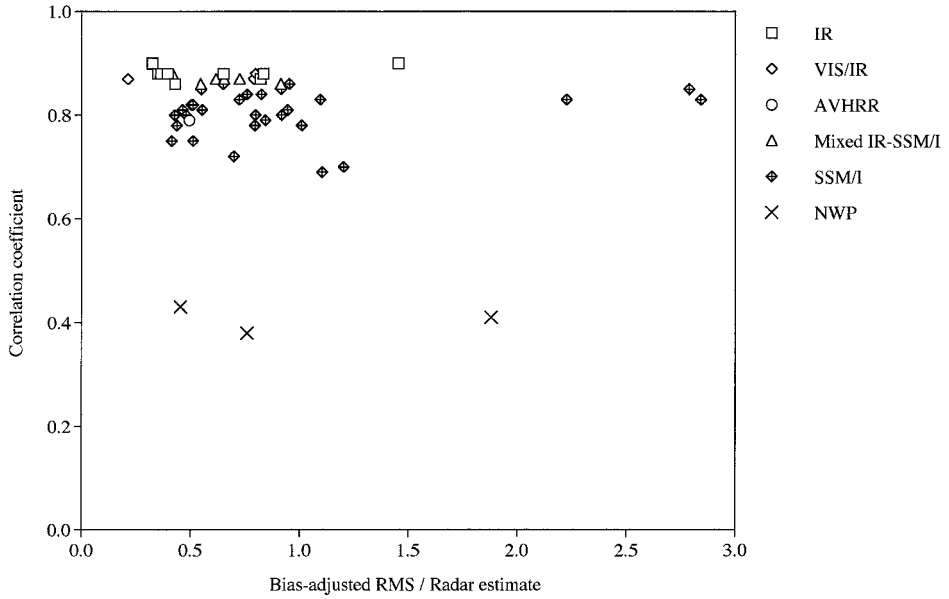

FIG. 4. Correlation coefficient of satellite-estimated and radar-estimated monthly rainfall vs normalized bias-adjusted rms difference.

differences, fall in the upper left portion of the plot. At monthly timescales, the skill of the geostationary (IR, VIS/IR, and mixed IR-SSM/I) algorithms exceeds slightly that of the AVHRR and SSM/I algorithms, with greater correlation coefficients and a tendency toward lower bias-adjusted rms differences. It appears that the advantage of superior temporal and spatial sampling in the geostationary algorithms outweighs the advantage of more physically direct measurements in the SSM/I algorithms, at least on timescales of up to a month.

b. Instantaneous rainfall

Estimates of instantaneous rainfall rate from all satellite algorithms were intercompared for a ''common set'' of grid boxes, that is, those for which all algorithms produced rainfall estimates. This process of intercomparing the ''lowest common denominator'' of instantaneous rain rate estimates ensured that the intercomparison statistics had comparable meaning for all types of algorithms. The ''common set'' was identical to the

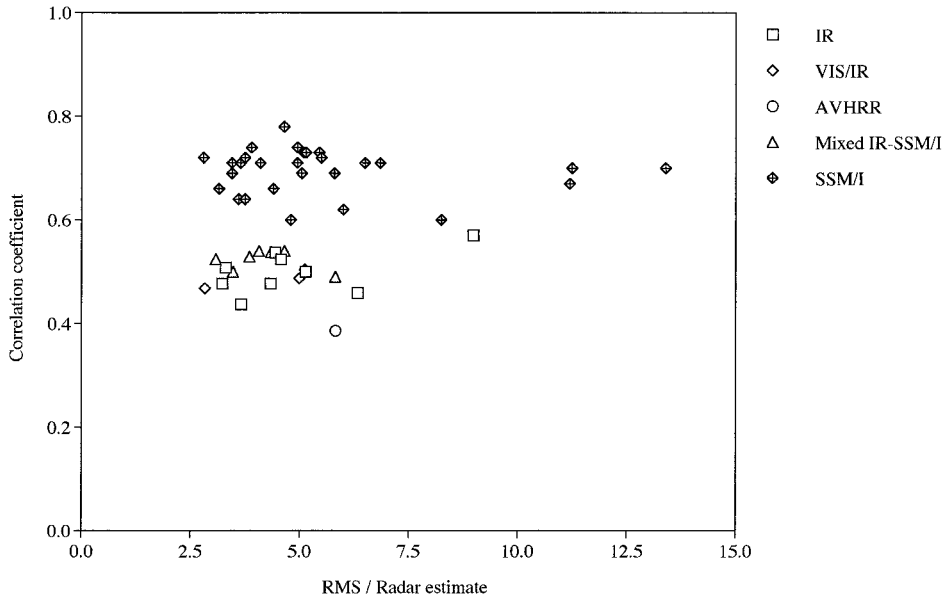

FIG. 5. Correlation coefficient of satellite-estimated and radar-estimated instantaneous rain rates vs normalized rms difference.

TABLE 5. Intercomparison statistics for instantaneous rain rates for the ''common set.''

Algorithm	Number of points	Mean radar (mm h^{-1})	Mean satellite (mm h^{-1})	Bias (mm h^{-1})	Ratio	Rms difference (mm h^{-1})	Correlation coefficient	POD	FAR	2 × 2 skill
IR algorithms										
AD5	1756	0.20	0.26	0.05	1.27	0.81	0.50	0.37	0.20	0.36
AD6	1756	0.20	0.28	0.08	1.39	0.82	0.52	0.38	0.17	0.39
AR1	1756	0.20	0.43	0.23	2.13	0.85	0.48	0.59	0.31	0.46
AR2	1756	0.20	0.29	0.08	1.42	0.66	0.48	0.59	0.31	0.46
AR3	1756	0.20	0.25	0.04	1.22	0.66	0.51	0.47	0.23	0.43
GA1	1756	0.20	0.52	0.32	2.61	0.98	0.52	0.84	0.55	0.24
JO1	1756	0.20	0.30	0.10	1.48	1.26	0.47	0.28	0.16	0.30
KR1	1756	0.20	0.90	0.70	4.51	1.78	0.58	0.87	0.50	0.33
MO1	1756	0.20	0.33	0.13	1.64	0.73	0.43	0.57	0.32	0.44
VIS/IR algorithms										
GA2	1756	0.20	0.50	0.30	2.50	0.98	0.53	0.81	0.53	0.27
HO1	1756	0.20	0.13	−0.07	0.67	0.60	0.50	0.61	0.42	0.36
KR2	1756	0.20	0.51	0.31	2.55	0.96	0.49	0.74	0.43	0.41
AVHRR algorithms										
IN1	4043	0.19	0.31	0.12	1.60	1.13	0.39	0.48	0.31	0.37
Mixed IR-SSM/I algorithms										
AD2	1756	0.20	0.30	0.10	1.48	1.06	0.49	0.25	0.17	0.26
AD4	1756	0.20	0.28	0.08	1.40	0.93	0.52	0.40	0.21	0.39
BE2	1743	0.20	0.26	0.06	1.29	0.63	0.53	0.54	0.34	0.40
BE3	1743	0.20	0.38	0.18	1.90	0.74	0.55	0.66	0.40	0.41
KM2	1756	0.20	0.26	0.06	1.32	0.68	0.50	0.49	0.23	0.44
KM4	1756	0.20	0.26	0.06	1.29	0.86	0.52	0.40	0.21	0.39
SH1	639	0.15	0.21	0.06	1.44	0.72	0.53	0.49	0.53	0.20
SSM/I algorithms										
AD1	1760	0.20	0.35	0.15	1.75	1.30	0.71	0.35	0.03	0.40
AO1	1760	0.20	0.26	0.06	1.29	0.73	0.71	0.48	0.05	0.53
AO2	1760	0.20	0.19	−0.01	0.94	0.69	0.71	0.31	0.02	0.36
BA0	1760	0.20	0.41	0.20	2.02	0.75	0.72	0.82	0.23	0.68
BA1	1760	0.20	0.29	0.09	1.44	0.73	0.71	0.51	0.06	0.55
BA2	1760	0.20	0.35	0.15	1.73	0.78	0.74	0.65	0.12	0.64
BA3	1760	0.20	0.48	0.28	2.39	0.99	0.71	0.72	0.21	0.63
BA4	1760	0.20	0.50	0.30	2.47	1.03	0.73	0.83	0.27	0.64
BA5	1760	0.20	0.87	0.67	4.34	2.68	0.70	0.82	0.28	0.62
BE1	1760	0.20	0.30	0.10	1.51	0.75	0.64	0.39	0.04	0.44
CH1	1760	0.20	0.25	0.05	1.24	0.56	0.72	0.74	0.18	0.67
FE1	1760	0.20	0.33	0.13	1.64	1.09	0.73	0.51	0.08	0.55
FE2	1760	0.20	0.43	0.23	2.14	1.65	0.60	0.57	0.11	0.58
FE3	1760	0.20	0.34	0.14	1.69	0.96	0.60	0.59	0.06	0.62
FE4	1760	0.20	0.33	0.13	1.64	0.99	0.74	0.59	0.08	0.62
FR1	1760	0.20	0.45	0.24	2.22	1.01	0.69	0.62	0.14	0.61
HA1	1055	0.18	0.28	0.11	1.60	1.08	0.62	0.32	0.06	0.35
IA1	1760	0.20	1.19	0.99	5.93	2.24	0.67	0.95	0.54	0.27
IA2	1760	0.20	1.18	0.98	5.89	2.25	0.70	0.93	0.56	0.24
KM1	1760	0.20	0.34	0.14	1.71	1.10	0.72	0.55	0.08	0.57
LI1	1760	0.20	0.21	0.01	1.05	0.69	0.69	0.40	0.05	0.45
MZ1	1760	0.20	0.41	0.21	2.02	1.16	0.69	0.51	0.08	0.54
PE1	1760	0.20	0.34	0.14	1.68	0.93	0.78	0.52	0.05	0.56
PE2	1760	0.20	0.38	0.18	1.89	1.02	0.73	0.54	0.06	0.58
PR1	1760	0.20	0.46	0.26	2.27	1.37	0.71	0.79	0.22	0.67
SC1	1663	0.19	0.27	0.08	1.41	0.82	0.71	0.76	0.22	0.66
SM1	1760	0.20	0.31	0.11	1.53	0.72	0.64	0.52	0.09	0.55
SM2	1760	0.20	0.22	0.02	1.11	0.63	0.66	0.58	0.09	0.60
WI1	1760	0.20	0.26	0.06	1.32	0.88	0.66	0.31	0.03	0.36

set of grid boxes containing SSM/I estimates (since for every SSM/I swath there was a corresponding GMS image measured within half an hour) and contained up to four images each day. Due to the inherent lag in overpass times between the NOAA and DMSP satellites, the intercomparison statistics for AVHRR algorithm IN1 were necessarily computed for a different sampling of data than the common set.

Table 5 and Fig. 5 present the intercomparison statistics for the satellite-estimated instantaneous rain rates.

TABLE 6. Mean interalgorithm correlation coefficients for (a) monthly rainfall estimates and (b) instantaneous rain-rate estimates. The number of algorithms in each group is given in parentheses. See text for detail of Table 6b.

(a) Monthly rainfall

	IR (9)	VIS/IR (3)	AVH-RR (1)	Mixed (9)	SSM/I (30)	NWP/GCM (4)	Clim (1)
IR	0.93	0.92	0.68	0.93	0.61	−0.09	−0.05
VIS/IR		0.94	0.67	0.92	0.64	−0.08	−0.09
AVHRR			1.00	0.68	0.47	−0.09	−0.07
Mixed				0.94	0.62	−0.10	−0.12
SSM/I					0.76	−0.02	−0.05
NWP						−0.10	−0.04
Clim							1.00

(b) Instantaneous rain rates

	IR (9)	VIS/IR (3)	AVH-RR (1)	Mixed (7)	SSM/I (29)
IR	0.72	0.72	0.56	0.77	0.59
VIS/IR	0.70	0.71	0.55	0.74	0.60
AVHRR	0.53	0.55	1.00	0.59	1.00
Mixed	0.74	0.72	0.56	0.84	0.70
SSM/I	0.54	0.58	1.00	0.64	0.79

As in the monthly intercomparison, the statistics were computed by pooling all estimates in space and time. The common set contained 1760 samples, with a mean radar-estimated rain rate over all grid boxes of 0.2 mm h^{-1}. Compared to the radar data, almost all of the satellite algorithms overestimated the rain rates, typically by a factor of 1.5, but a few by more than four times. Rms differences varied from 0.6 to 2.7 mm h^{-1}, with the majority of both the IR-based and SSM/I algorithms producing rms differences between three and six times the average radar-estimated rainfall.

For instantaneous rainfall, the IR, VIS/IR, AVHRR, and mixed algorithms had satellite–radar correlation coefficients ranging from 0.39 to 0.58. The SSM/I algorithms performed much better than the IR-based algorithms, with correlation coefficients in the range of 0.60–0.78 for instantaneous rain rates. Within the set of SSM/I algorithms, those that were primarily emission-based and did not use information from the 85-GHz channels showed slightly lower correlations with the radar observations than did those algorithms that included the 85-GHz scattering signal. The statistical significance tests indicate that, for this large number of samples, correlation coefficients differing by more than about 0.04 can be considered statistically distinct at the 95% confidence level. This result shows that the microwave algorithms generally estimate instantaneous rain rates with much greater skill than do the more empirical algorithms that depend on infrared and visible data. The mixed algorithms, although adjusted using SSM/I rainfall analyses, showed similar performance to the IR and VIS/IR algorithms.

The 2×2 skill score measures an algorithm's ability to correctly diagnose the presence or absence of rain, with a score of 1.0 indicating perfect rain detection. Of the algorithms using infrared and visible imagery, AR1 (GPI) showed the greatest skill in delineating raining areas from nonraining areas, with a skill score of 0.46. This reaffirms the utility of infrared brightness temperatures in detecting precipitation in the Tropics. Higher 2×2 skill scores were achieved by some of the SSM/I algorithms, with values of up to 0.68. In general, the microwave algorithms showed greater skill than the IR-based algorithms in delineating raining from nonraining areas, which contributed to their greater success in estimating instantaneous rain rates.

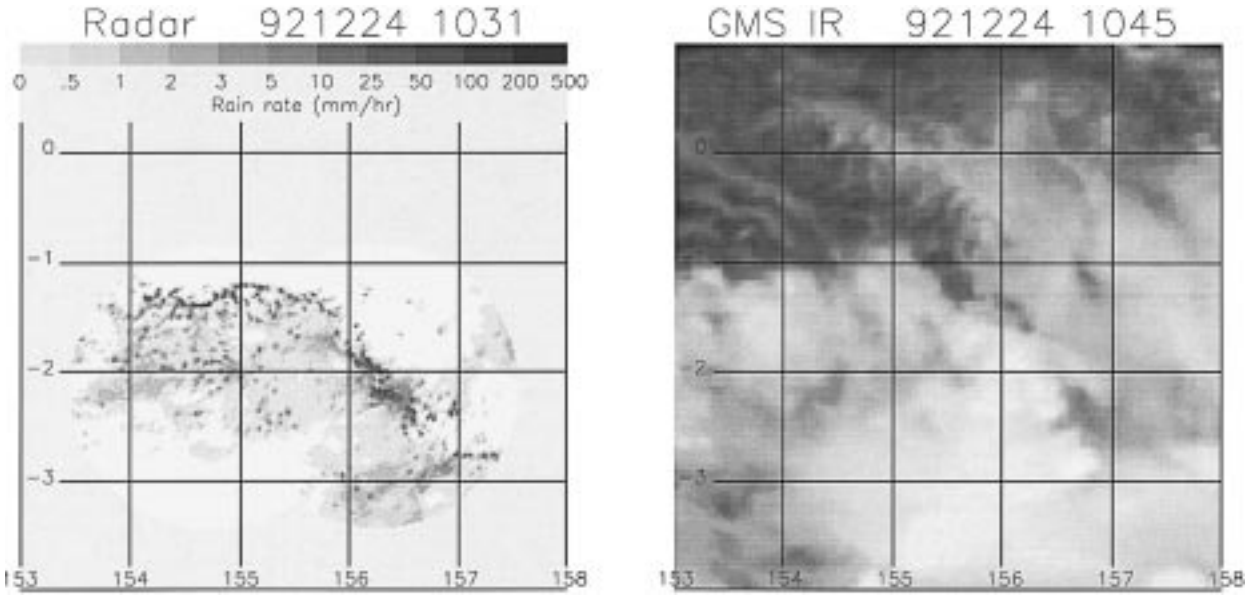

FIG. 6. (a) Radar rain rates at 1031 UTC and (b) GMS infrared imagery at 1045 UTC 24 December 1992 for the AIP-3 region.

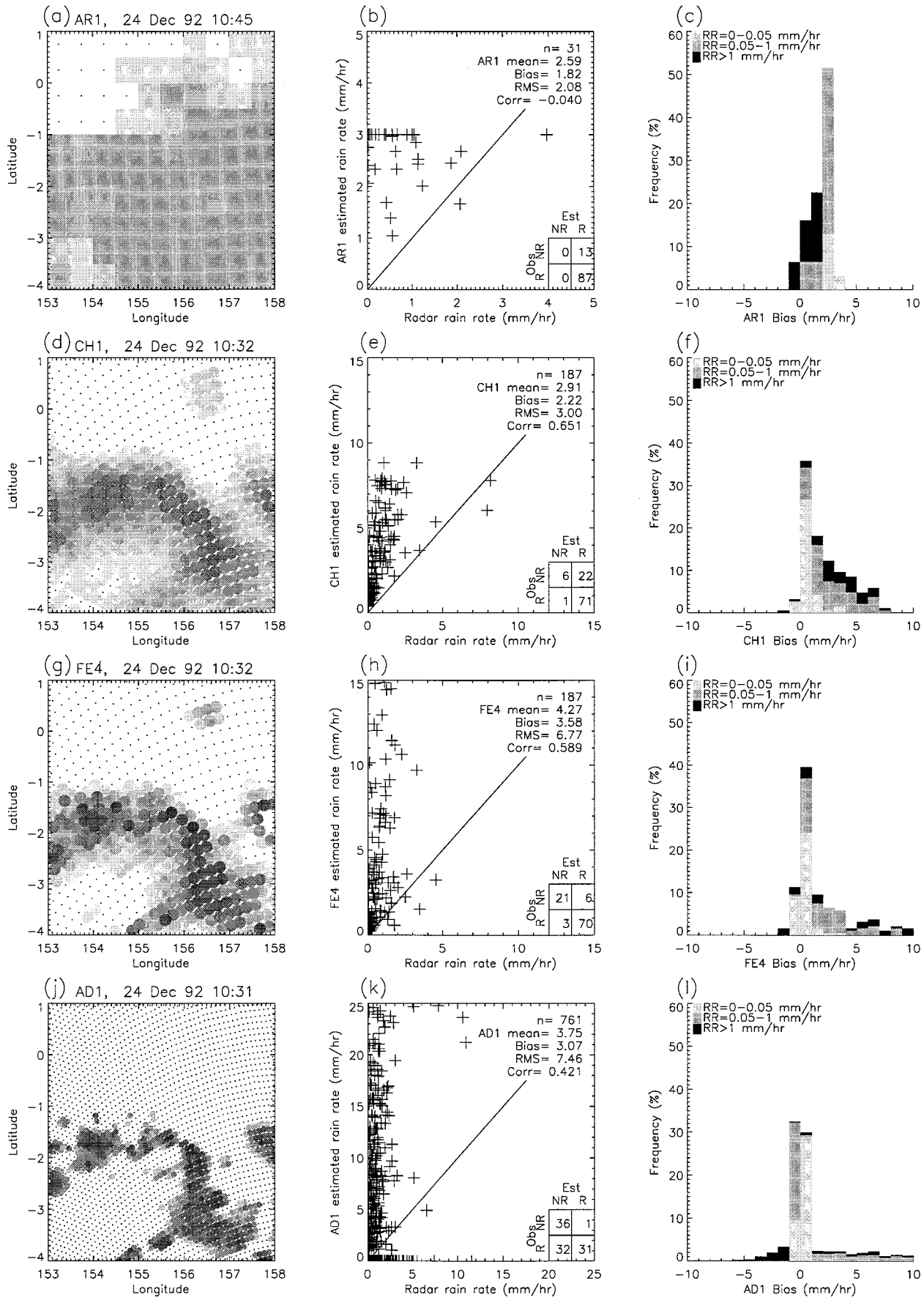

c. Interalgorithm correlations

The similarities between the algorithms can be assessed by computing the correlations between their respective estimates. Mean interalgorithm correlation coefficients are given in Table 6 for monthly and instantaneous rainfall. For each pair of algorithms, interalgorithm correlation coefficients were computed using several thousand gridded instantaneous rain rate estimates or 400 calendar monthly rainfall estimates. These were then averaged for each combination of algorithm types. In Table 6b the values to the lower left of the diagonal represent ''wet'' correlations; that is, correlations were computed using samples in which at least one of the algorithms estimated rain. The correlations in the upper right of the table were computed from all estimates.

Table 6 indicates that the IR-based algorithms are similar as a group and the SSM/I algorithms are also similar as a group, while the correlations between algorithms of different types are lower. The relative similarity of the IR-based algorithms, especially for monthly rainfall, is hardly surprising since they all relate rainfall to cloud T_B. The SSM/I algorithms correlate extremely highly with each other for instantaneous rain rates, which may be surprising at first, considering the variety of approaches that are used to estimate rainfall from SSM/I brightness temperatures (Table 2; Wilheit et al. 1994). Even pure microwave emission algorithms such as IA1 and WI1 showed remarkable similarity to pure scattering algorithms such as AD1, BA2, and PE2 (not shown). Most of the SSM/I algorithms use polarization or scattering indices to indicate the presence of rain (see Table 2), which accounts for much of the similarity. Except for the ECMWF model, the monthly NWP and GCM rainfall predictions correlated negligibly with the satellite estimates, as did climatology.

5. Case studies

In this section we show examples of four algorithms' estimates of instantaneous rain rates for two case studies. The two cases examined, 24 December 1992 and 15 February 1993, provide good examples of both convective and widespread stratiform rainfall. In doing this we hope to better understand the behavior of the algorithms, as well as gain further insight into the differences between them.

The four algorithms examined here (AR1, CH1, FE4, and AD1) are familiar techniques in the satellite rainfall community and are currently being used to produce global rainfall climatologies for the wider scientific community. The first, AR1, is the well-known GOES Precipitation Index (GPI) of Arkin and Meisner (1987). Although it was intended to be used on large timescales (monthly) and spatial scales ($\geq 2.5°$), it has demonstrated usefulness in providing instantaneous estimates of rain area (e.g., Puri and Davidson 1992). The GPI rain rate is computed simply as the fraction of pixels in a region with infrared T_B of 235 K or lower, multiplied by a rain rate of 3 mm h^{-1} to obtain the aerial-average rain rate. The GPI is used by the GPCP to provide estimates of rainfall over land and water between 40°N and 40°S latitude (Arkin and Xie 1994).

The second algorithm, CH1, is a modification of the SSM/I emission algorithm described by Wilheit et al. (1991), which is used to provide global oceanic rainfall estimates for the GPCP. The average freezing level, determined from a scattergram of SSM/I brightness temperatures, is used along with measurements from the low-frequency channels to estimate the rain rate using output from radiative transfer calculations and a simple cloud model. If the signal at 85 GHz shows strong scattering, the emission estimates are replaced by scattering estimates.

FE4, a scattering-based SSM/I algorithm, is a revised version of the algorithm described by Ferraro and Marks (1995). It is used by NOAA to provide global monthly rainfall estimates, which are available on the Internet, and also contributes estimates of rainfall over land to the GPCP (WCRP 1995). The assumption is made that the rain layer extends above the freezing level and thus produces an observed depression in the 85-GHz brightness temperature. A scattering index is computed from a selection of SSM/I channels, then used both to indicate the presence of rain and to estimate the rain rate using an exponential function.

The fourth algorithm shown in the case studies is AD1, which is the modified Goddard Scattering Algorithm (GSCAT-2) (Adler et al. 1993, 1994). Estimates of instantaneous rain rates calculated using the GSCAT-2 algorithm are routinely produced at Marshall Space Flight Center as part of the SSM/I Pathfinder dataset, which is available via the Internet. After delineating raining and nonraining areas using channels at 37 and 85 GHz, the rain rates are estimated as a linear function of the horizontally polarized 85-GHz brightness temperature.

a. 24 December 1992

Figure 6a shows the radar rain rates at 1031 UTC 24 December 1992. These observations were made during the mature phase of a mesoscale convective system. The image is characterized by widespread stratiform precip-

←

FIG. 7. Satellite estimated rain rates, scatterplots of satellite vs radar rain rates, and histograms of bias values for four algorithms: (a)–(c) AR1, (d)–(f) CH1, (g)–(i) FE4, and (j)–(l) AD1, for the rainfall case of 24 December 1992. The grayscale is the same as in Fig. 6a.

TABLE 7. Intercomparison statistics for instantaneous rain rates for the case study of 24 December 1992, for (a) pixel resolution and (b) 0.5° resolution.

Algorithm	Number of points	Mean radar (mm h^{-1})	Mean satellite (mm h^{-1})	Bias (mm h^{-1})	Ratio	Rms difference (mm h^{-1})	Correlation coefficient	POD	FAR	2 × 2 skill
(a) Pixel resolution										
AR1	31	0.77	2.60	1.83	3.39	2.08	−0.04	1.00	0.13	0.00
CH1	187	0.69	2.91	2.31	4.21	3.00	0.65	0.99	0.24	0.26
FE4	187	0.69	4.27	3.67	6.18	6.77	0.59	0.96	0.08	0.76
AD1	760	0.59	3.76	3.17	5.49	7.46	0.42	0.49	0.03	0.39
(b) Half-degree resolution										
AR1	31	0.77	2.60	1.83	3.39	2.08	−0.04	1.00	0.13	0.00
CH1	30	0.89	3.05	2.16	3.42	2.70	0.70	1.00	0.10	0.37
FE4	30	0.89	4.60	3.71	5.16	5.57	0.65	1.00	0.04	0.84
AD1	30	0.89	4.29	3.40	4.81	6.16	0.62	0.89	0.04	0.52

itation within which are embedded numerous cumulus convective cells. In this case the stratiform rain flux exceeded the convective rain flux (Carey et al. 1994). The accompanying GMS IR image from 1045 UTC is shown in Fig. 6b.

Intercomparison of the algorithms is shown in Fig. 7 and in Table 7. The leftmost column in Fig. 7 contains plots of satellite-estimated rain rates at full pixel resolution. (Note: the AR1 algorithm, like most IR-based algorithms, can produce rain rates at the GMS 5-km pixel scale; Fig. 7 shows the 0.5° gridded estimates that were produced for use in AIP-3.) Scatterplots show the satellite-estimated versus radar-estimated rain rates as well as the 1:1 line and a rain/no rain contingency table in the lower right corner of each plot. The rightmost column contains histograms of the bias, that is, the pixel-by-pixel difference between the satellite-estimated and radar rain rates, with the frequencies differentiated into three ranges of radar rain rates. Table 7 gives the intercomparison statistics for estimates both at pixel resolution and averaged onto the 0.5° grid.

Compared to the radar estimates of rain rate, all four of the algorithms overestimated the rainfall falling in the area viewed by the radars. The AR1 (GPI) estimated rainfall field for this scene was fairly homogeneous with rain rates at or near the maximum possible for the algorithm (3 mm h^{-1}). This algorithm diagnosed rain from the cold IR T_B associated with extensive cirrus cloud cover (Fig. 6b), leading to an overestimate of rain area and almost no spatial correlation with the observations. Because the GPI rain rates were fairly conservative, the bias, ratio, and rms differences were lower than those evaluated for the other three algorithms at 0.5° grid resolution.

SSM/I emission algorithm CH1 also overestimated the rain area, although the rain pattern was much better represented. The correlation of 0.65 at pixel resolution (0.70 at 0.5° resolution) was the highest achieved by the four algorithms. Figures 7e and 7f show that bias was greatest for the heaviest observed rain rates, unlike the AR1 analysis. The stratiform rain extent and intensity were overestimated by CH1; this would occur if the algorithm was sensing rainfall that evaporated before reaching the surface.

The greatest skill in delineating the rain area in this case was shown by scattering algorithm FE4, with a 2 × 2 skill score of 0.76. This algorithm also produced the greatest positive bias, overestimating the mean rain rate (intensity) by a factor of 6. Algorithm AD1 (GSCAT-2), also a scattering-based algorithm, also significantly overestimated the rain intensity. AD1 used a more selective criterion for determining the pixels likely to be raining, which resulted in a smaller rain area than was observed (the probability of detection was 0.49) but also a reduction in the mean bias. When averaged onto the 0.5° grid, the FE4 and AD1 algorithms produced quite similar intercomparison statistics.

In summary, for this case of widespread convective and stratiform rain on 24 December 1992 the rainfall was overestimated by all of the algorithms to varying degrees. The IR algorithm could not detect the spatial variations in rainfall, while the SSM/I algorithms successfully reproduced the spatial pattern of observed rainfall. The scattering algorithms particularly overestimated the magnitudes of the rain rates.

b. 15 February 1993

This case, from 0711 UTC 15 February 1993, contained clusters of scattered convection throughout the AIP-3 region. The radar rain map (Fig. 8a) shows several storms in various stages of development and maturity, some with local rain rates exceeding 70 mm h^{-1}. The associated GMS IR image from 0745 UTC shows significant spatial variability, with large cirrus anvils associated with some of the storms. The intercomparison statistics for this case are given in Table 8.

Figure 9 shows that the AR1 (GPI) algorithm estimated rainfall in all grid boxes seen by the radar but with a great deal more spatial variability than in the previous case. The rain pattern was well represented, resulting in a correlation coefficient of 0.48, although the average rain rates were too great by a factor of ~2 when compared to the radar estimates. This led to AR1

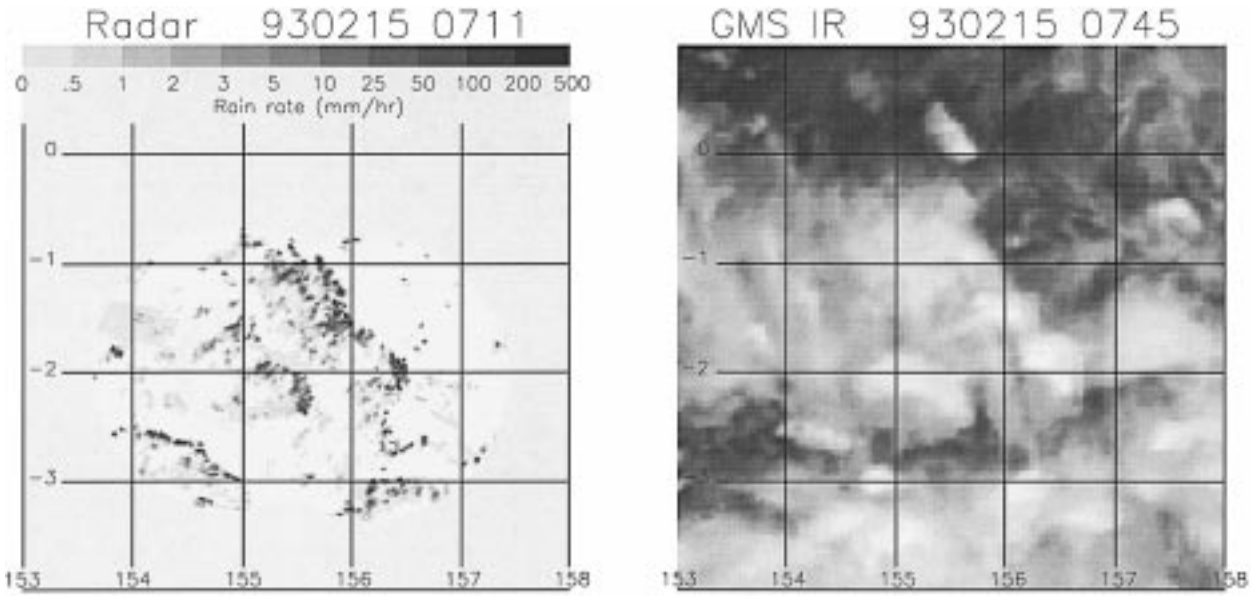

FIG. 8. As in Fig. 6 but for 0711 UTC 15 February 1993.

having the largest bias and rms difference of all the algorithms on the 0.5° grid. However, this algorithm provided the most accurate estimates at high rainfall rates.

The three SSM/I algorithms all underestimated the rainfall in this scattred convection. The emission algorithm, CH1, overestimated the rain area by about 20%. However, the rain rates in many of the pixels with heavy rain were underestimated by several millimeters per hour (Figs. 9e,f). Averaging onto the 0.5° grid smooths out these offsetting errors, resulting in a correlation coefficient of 0.76, the highest of the four algorithms.

Scattering algorithms FE4 and AD1 (GSCAT-2) underestimated the rain area by 36% and 83%, respectively. A strong scattering signal did not seem to be present in many of the pixels that had observed heavy rain rates; AD1 detected almost no rain in the western one-third of the radar imagery. One reason for the difference in estimated rain extent between FE4 and AD1 is that the latter has a rain rate detection cutoff of 1 mm h^{-1}, and thus does not analyze rainfall at the lowest end of the scale. At the high end of the scale AD1 and FE4 were more successful than CH1 in diagnosing heavy rain rates. The rms differences for the SSM/I algorithms were significantly lower than that of the geostationary algorithm when estimates were averaged onto the 0.5° grid, and the correlation coefficients significantly higher.

In summary, when compared to the radar estimates in this case the IR algorithm overestimated the rain while the SSM/I algorithms underestimated the rain. AR1 (GPI) showed significant skill in diagnosing the rain pattern. For the CH1 emission algorithm the rain area was too large while the estimated rain rates were too small. The SSM/I scattering algorithms underestimated the rain area while producing reasonable rain

TABLE 8. Intercomparison statistics for instantaneous rain rates for the case study of 15 February 1993, for (a) pixel resolution and (b) 0.5° resolution.

Algorithm	Number of points	Mean radar (mm h^{-1})	Mean satellite (mm h^{-1})	Bias (mm h^{-1})	Ratio	Rms difference (mm h^{-1})	Correlation coefficient	POD	FAR	2 × 2 skill
(a) Pixel resolution										
AR1	24	1.04	1.71	0.68	1.66	1.36	0.33	0.96	0.00	0.00
CH1	148	0.98	0.76	−0.22	0.78	1.95	0.48	0.91	0.19	0.43
FE4	148	0.98	0.60	−0.38	0.61	1.96	0.46	0.64	0.00	0.51
AD1	620	1.02	0.53	−0.49	0.52	3.17	0.32	0.16	0.05	0.14
(b) Half-degree resolution										
AR1	24	1.04	1.71	0.68	1.66	1.36	0.33	0.96	0.00	0.00
CH1	24	0.82	0.75	−0.07	0.92	0.65	0.77	1.00	0.17	0.28
FE4	24	0.82	0.62	−0.19	0.76	0.76	0.66	0.79	0.17	0.18
AD1	24	0.82	0.55	−0.26	0.68	0.90	0.66	0.53	0.17	0.08

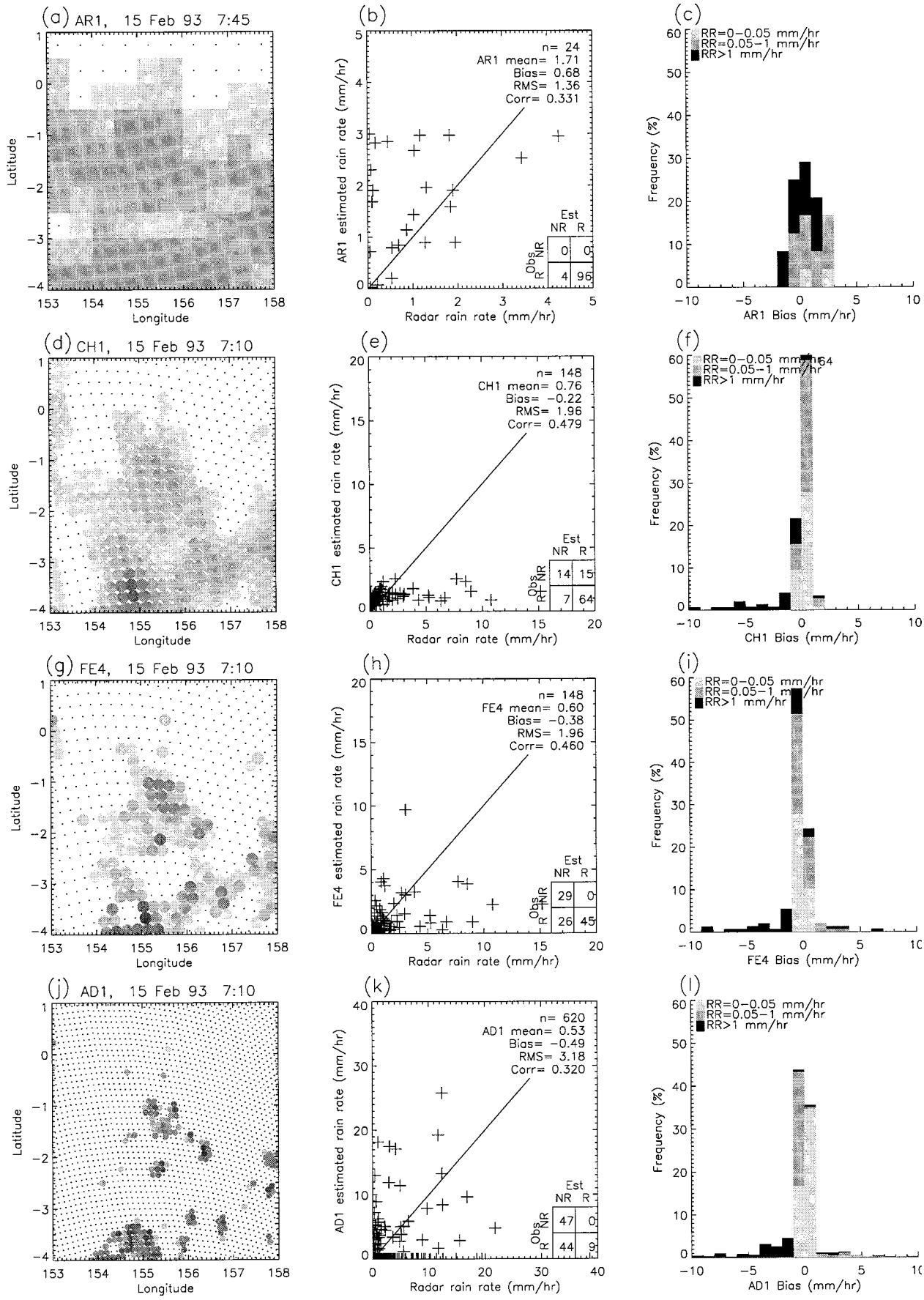

rates. Nevertheless, all three SSM/I algorithms produced 0.5° gridded estimates that correlated well with the observations.

6. Summary and conclusions

AIP-3 evaluated over 50 satellite rainfall algorithms for a 5° square region in the western Pacific Ocean during TOGA COARE, November 1992–February 1993. The satellite algorithms used GMS VIS/IR, AVHRR, and SSM/I data to estimate rainfall on both instantaneous and monthly timescales. Validation data came from two calibrated shipboard Doppler radars measuring rainfall every 10 minutes. All radar observations and satellite rainfall estimates were mapped onto a 0.5° grid to compute intercomparison statistics for the algorithms.

The most important findings of the AIP-3 experiment are the following.

1) Most of the satellite algorithms estimated rainfall amounts that were greater than those estimated by the radars, with mean ratio values ranging from 0.6 to 5.1 and a median value of 1.3. There were no categorical differences in bias between algorithms of different types.
2) The median value of the ratio of satellite-estimated to radar-estimated rainfall differed substantially for the three cruises, with values of 0.75, 1.7, and 1.3, respectively. This is due to the different rainfall regimes encountered on the cruises. The satellite algorithms tended to overestimate rain in heavy rain situations.
3) At monthly timescales, algorithms using geostationary data (IR, VIS/IR, and mixed IR-SSM/I algorithms) exhibited slightly higher correlations with the radar estimates (0.86–0.90) than did estimates based on AVHRR or SSM/I data alone (0.69–0.86). This is a result of the superior spatial and temporal sampling possible using geostationary satellites. Due to the small number of monthly samples, differences of less than about 0.15 between correlation coefficients of the various algorithms are not statistically significant.
4) Instantaneous correlations between SSM/I estimates and radar were substantially higher than those of any other type of algorithm, with values in the range of 0.60–0.78. In fact, the lowest of the SSM/I correlations was higher than any other. The statistical significance tests indicated that correlations differing by only a few percent can be considered statistically different with a high degree of confidence. The relative success of the SSM/I algorithms compared to the IR-based algorithms appears to be related in large part to their superiority in distinguishing raining from nonraining areas. Inclusion of the scattering signal at 85 GHz appears to improve the rain rate estimates relative to those of the emission algorithms.
5) The mixed IR–SSM/I algorithms evaluated in AIP-3 had biases, rms difference, and correlation coefficients with the radar estimates that were similar to those of the IR-only algorithms. In order for a mixed IR–SSM/I algorithm to perform better than the IR-only algorithm incorporated within, it must be coupled with a SSM/I algorithm having a significantly smaller mean bias.
6) The NWP models overestimated the monthly rainfall during AIP-3. Although they had similar biases and rms differences to the satellite algorithms, the models exhibited much poorer correlations with the radar data (~0.4).

It is useful to compare the results of AIP-3 with the results of other satellite rainfall intercomparison studies. The above conclusions, except for (6), reinforce the conclusions of AIP-1. Ebert et al. (1996) found that although the algorithms in AIP-3 showed a higher mean bias, their normalized monthly rms differences were similar to those produced in AIP-1 (summertime rain in Japan) and AIP-2 (springtime precipitation in western Europe). The monthly correlation coefficients of satellite estimates with radar estimates were substantially greater in AIP-3 than in the other two experiments. This is in spite of the fact that the grid boxes in AIP-3 were less than one-quarter the size of those used in AIP-1 and AIP-2, increasing the effects of random errors. The performance of the SSM/I algorithms in AIP-3 is similar to that shown in the western Pacific in PIP-1 (Barrett et al. 1994).

For instantaneous rain rates the IR-based algorithms in AIP-3 had normalized rms differences that were comparable to those found in AIP-1 and much better than those found in AIP-2 (Ebert et al. 1996). The correlation coefficients for the IR-based algorithms in AIP-3 were twice as great as the AIP-1 and AIP-2 values, largely because IR-based algorithms are much better suited to estimate rainfall in tropical convection than in other regimes. The SSM/I algorithms in AIP-3 had greater rms differences and slightly lower correlation coefficients than were found in AIP-1, but these differences can be explained partly by the difference in scale. When the instantaneous rain rate estimates are validated on a 1° grid (comparable to the 1.25° grid used in AIP-1), the rms differences decrease by 18% and the correlation coefficients improve by 15%, making the AIP-3 correlations as high as those in AIP-1.

At SSM/I pixel scale, the algorithms in PIP-2 had

←

FIG. 9. As in Fig. 7 but for the rainfall case of 15 February 1993.

normalized rms differences of about 1.5 mm h^{-1} and correlation coefficients with the observations of about 0.5 for convective systems over the ocean (Smith et al. 1996). The SSM/I algorithms examined in the two case studies presented here had greater normalized rms differences (particularly for the 24 December 1992 case) but similar correlation coefficients (0.42–0.65).

The differences in algorithm performance between the intercomparison experiments are due to several factors. The most obvious factor is the rainfall regime. This is clearly illustrated by the contrast in performance of the IR-based algorithms in the tropical western Pacific as compared to western Europe in spring. The spatial scale of the analysis influences the validation statistics as spatial averaging smooths out much of the random error. The quality of the validation data is an important factor. This led to an enormous quality control effort in AIP-2 (Allam et al. 1993) and a reanalysis of the radar observations in AIP-3 (Short et al. 1997). Finally, it is expected that the relative success of satellite rainfall algorithms in AIP-3 is partly due to improvements in the algorithms themselves with time, as the results of previous intercomparison experiments have been used to refine existing algorithms and develop new ones.

There remain several areas of improvement for satellite rainfall estimation. These include improved delineation of raining and nonraining areas, possible classification of rain into convective and stratiform types, improvements to the rain physics used by the cloud models in some SSM/I algorithms, and further efforts to combine observations from different spectral regions and observing platforms.

Acknowledgments. Thanks are due to JMA and the University of Hawaii for supplying GMS imagery to augment the Bureau of Meteorology's archives during TOGA COARE, J. Wilkerson for supplying the SSM/I data, and G. Wick for providing AVHRR data. Thanks also to M. Saiki (Japan Meteorological Agency), J. Janowiak (National Meteorological Center), and the late Bill Heckley (European Centre for Medium-Range Weather Forecasts) for supplying the model analyses and precipitation forecasts used in this project, M. Morrissey and M. Shafer for providing the Pacific atoll rain gauge dataset, and K. Arpe for contributing GCM monthly precipitation estimates. We are very grateful to D. Short, P. Kucera, and B. Ferrier, who painstakingly prepared the radar rainmaps required to validate the satellite estimates. This project was made much easier by the previous work done by T. Lee and J. Janowiak for AIP-1, and R. Allam and G. Holpin for AIP-2. Superb technical assistance was given by D. Howard, M. Perkins, and P. Meighen. Thanks are also due to the anonymous reviewers whose comments improved the quality of this paper.

REFERENCES

Adler, R. F., and A. J. Negri, 1988: A satellite infrared technique to estimate tropical convective and stratiform rainfall. *J. Appl. Meteor.*, **27,** 30–51.

——, ——, P. R. Keehn, and I. M. Hakkarinen, 1993: Estimation of monthly rainfall over Japan and surrounding waters from a combination of low-orbit microwave and geosynchronous IR data. *J. Appl. Meteor.*, **32,** 335–356.

——, G. J. Huffman, and P. R. Keehn, 1994: Global tropical rain estimates from microwave-adjusted geosynchronous IR data. *Remote Sens. Rev.*, **11,** 125–152.

Allam, R. E., G. Holpin, P. Jackson, and G. L. Liberti, 1993: Second Algorithm Intercomparison Project of the Global Precipitation Climatology Project (AIP-2), U.K. and Northwest Europe, February–April 1991. Pre-Workshop Rep. Satellite Image Applications Group, U.K. Meteorological Office, 439 pp. [Available from Satellite Image Applications Group, U.K. Meteorological Office, Bracknell, Berkshire, RG12 2SZ, United Kingdom.]

Aonashi, K., A. Shibata, and G. Liu, 1996: An over-ocean precipitation retrieval using SSM/I multichannel brightness temperatures. *J. Meteor. Soc. Japan*, **74,** 617–637.

Arkin, P. A., and B. N. Meisner, 1987: The relationship between large-scale convective rainfall and cold cloud over the Western Hemisphere during 1982–84. *Mon. Wea. Rev.*, **115,** 51–74.

——, and P. Xie, 1994: The Global Precipitation Climatology Project: First Algorithm Intercomparison Project. *Bull. Amer. Meteor. Soc.*, **75,** 401–419.

Barrett, E. C., R. F. Adler, K. Arpe, P. Bauer, W. Berg, A. Chang, R. Ferraro, J. Ferriday, S. Goodman, Y. Hong, J. Janowiak, C. Kidd, D. Kniveton, M. Morrissey, W. Olson, G. Petty, B. Rudolf, A. Shibata, E. Smith, and R. Spencer, 1994: The First WetNet Precipitation Intercomparison Project (PIP-1): Interpretation of results. *Remote Sens. Rev.*, **11,** 303–373.

Basili, P., P. Ciotti, G. d'Auria, F. S. Marzano, and N. Pierdicca, 1995: Microwave radiometry characterization of precipitating clouds. *Microwave Radiometry of the Environment*, D. Solimini, Ed., VSP International Scientific Publishers, 253–263.

Bauer, P., and P. Schluessel, 1993: Rainfall, total water, ice water, and water vapor over sea from polarized microwave simulations and Special Sensor Microwave/Imager data. *J. Geophys. Res.*, **98,** 20 737–20 759.

Berg, W., 1994: Precipitation retrieval during TOGA COARE using a combination of SSM/I and GMS data with application to climate studies. Preprints, *Seventh Conf. on Satellite Meteorology and Oceanography*, Monterey, CA, Amer. Meteor. Soc., 67–70.

——, and R. Chase, 1992: Determination of mean rainfall from the Special Sensor Microwave/Imager (SSM/I) using a mixed lognormal distribution. *J. Atmos. Oceanic Technol.*, **9,** 129–141.

Carey, L. D., S. A. Rutledge, and R.H. Johnson, 1994: Heat and moisture budget over the TOGA COARE IFA during the mature phase of the 24 December 1992 mesoscale convective system. Preprints, *Sixth Conf. on Mesoscale Processes*, Portland, OR, Amer. Meteor. Soc., 5–8.

Churchill, D. D., and R. A. Houze, 1984: Development and structure of winter monsoon cloud clusters on 10 December 1978. *J. Atmos. Sci.*, **41,** 993–960.

Ebert, E. E., 1996: Results of the 3rd Algorithm Intercomparison Project (AIP-3) of the Global Precipitation Climatology Project (GPCP). Revision 1. BMRC Research Rep. No. 55, 299 pp. [Available from Bureau of Meteorology Research Centre, GPO Box 1289K, Melbourne, Australia 3000.]

——, M. J. Manton, P. A. Arkin, R. J. Allam, G. E. Holpin, and A. Gruber, 1996: Results from the GPCP Algorithm Intercomparison Projects. *Bull Amer. Meteor. Soc.*, **77,** 2875–2887.

Ferraro, R. R., and G. F. Marks, 1995: The development of SSM/I rain-rate retrieval algorithms using ground-based radar measurements. *J. Atmos. Oceanic Technol.*, **12,** 755–770.

Ferriday, J. G., and S. K. Avery, 1994: Passive microwave remote

sensing of rainfall with SSM/I: Algorithm development and implementation. *J. Appl. Meteor.,* **33,** 1587–1596.

Fiore, J. B., and N. C. Grody, 1990: A classification algorithm for monitoring snow cover and precipitation using SSM/I measurements. Preprints, *Fifth Conf. on Satellite Meteorology and Oceanography,* London, United Kingdom, Amer. Meteor. Soc., 237–240.

Goodman, B., P. Menzel, D. Martin, and E. Cutrim, 1993: A nonlinear algorithm for estimating three-hourly rain rates over Amazonia from GOES/VISSR observations. *Remote Sens. Rev.,* **10,** 169–177.

Grassotti, C., and L. Garand, 1994: Classification-based rainfall estimation using satellite data and numerical forecast model fields. *J. Appl. Meteor.,* **33,** 159–178.

Grody, N. C., 1991: Classification of snow cover and precipitation using the Special Sensor Microwave/Imager (SSM/I). *J. Geophys. Res.,* **96,** 7423–7435.

Hogg, W. D., 1990: Comparison of some VIS/IR rainfall estimation techniques. Preprints, *Fifth Conf. on Satellite Meteorology and Oceanography,* London, United Kingdom, Amer. Meteor. Soc., 287–291.

Inoue, T., 1987: An instantaneous delineation of convective rainfall areas using split-window data of NOAA-7 AVHRR. *J. Meteor. Soc. Japan,* **65,** 469–481.

Janowiak, J. E., 1992: Tropical rainfall: A comparison of satellite-derived rainfall estimates with model precipitation forecasts, climatologies, and observations. *Mon. Wea. Rev.,* **120,** 448–462.

Jobard, I., and M. Desbois, 1994: Satellite estimation of the tropical precipitation using the METEOSAT and SSM/I data. *Atmos. Res.,* **34,** 285–298.

Kummerow, C., and L. Giglio, 1994: A passive microwave technique for estimating rainfall and vertical structure information from space. Part I: Algorithm description. *J. Appl. Meteor.,* **33,** 3–18.

Lee, T. H., J. E., Janowiak, and P. A. Arkin, 1991: *Atlas of Products from the Algorithm Intercomparison Project 1: Japan and Surrounding Oceanic Regions, June–August 1989.* University Corporation for Atmospheric Research, 131 pp. [Available from the Climate Analysis Center, NOAA, 5200 Auth Road, Camp Springs, MD 20746-4304.]

Liu, G., and J. A. Curry, 1992: Retrieval of precipitation from satellite microwave measurement using both emission and scattering. *J. Geophys. Res.,* **97,** 9959–9974.

——, ——, and R.-S. Sheu, 1995: Classification of clouds over the western equatorial Pacific Ocean using combined infrared and microwave satellite data. *J. Geophys. Res.,* **100,** 13 811–13 826.

Marzano, F. S., A. Mugnai, N. Pierdicca, E. A. Smith, J. Turk, and J. Vivekanandanan, 1995: Precipitation profile retrieval from airborne microwave radiometers: A case study over ocean during CaPE. *Microwave Radiometry of the Environment,* D. Solimini, Ed., VSP International Scientific Publishing, 264–274.

McBride, J. L., N. E. Davidson, K. Puri, and G. C. Tyrell, 1995: The flow during TOGA COARE as diagnosed by the BMRC Tropical Analysis and Prediction System. *Mon. Wea. Rev.,* **123,** 717–736.

Morrissey, M. L., and J. S. Greene, 1991: The Pacific Atoll raingage data set. JIMAR Contribution No. 91-242, 45 pp. [Available from School of Ocean and Earth Science and Technology, University of Hawaii, Honolulu, HI 96822.]

——, W. F. Krajewski, and M. J. McPhaden, 1994: Estimating rainfall in the Tropics using the fractional time raining. *J. Appl. Meteor.,* **33,** 387–393.

Negri, J. J., R. F. Adler, and P. J. Wetzel, 1984: Rain estimation from satellites: An examination of the Griffith–Woodley technique. *J. Climate Appl. Meteor.,* **23,** 102–116.

Petty, G. W., and D. R. Stettner, 1994: A new inversion-based algorithm for retrieval of over-water rain rate from SSM/I multichannel imagery. Preprints, *Seventh Conf. on Satellite Meteorology and Oceanography,* Monterey, CA, Amer. Meteor. Soc., 144–147.

Puri, K., and N. E. Davidson, 1992: The use of infrared satellite cloud imagery data as proxy data for moisture and diabatic heating in data assimilation. *Mon. Wea. Rev.,* **120,** 2329–2341.

Rasmussen, E. M., and P. A. Arkin, 1993: A global view of large-scale precipitation variability. *J. Climate,* **6,** 1495–1522.

Richards, F., and P. Arkin, 1981: On the relationship between satellite-observed cloud cover and precipitation. *Mon. Wea. Rev.,* **109,** 1081–1093.

Rosenfeld, D., and G. Gutman, 1994: Retrieving microphysical properties near the tops of potential rain clouds by multispectral analysis of AVHRR data. *Atmos. Res.,* **34,** 259–283.

Shinoda, T., and R. Lukas, 1995: Lagrangian mixed layer modeling of the western equatorial Pacific. *J. Geophys. Res.,* **100,** 2523–2541.

Short, D., P. Kucera, B. Ferrier, J. Gerlach, S. Rutledge, and O. Thiele, 1997: Shipboard radar rainfall patterns within the TOGA COARE IFA. *Bull. Amer. Meteor. Soc.,* **78,** 2817–2836.

Smith, E., X. Xiang, A. Mugnai, and G. I. Tripoli, 1994: Design of an inversion-based precipitation profile retrieval algorithm using an explicit cloud model for initial guess microphysics. *Meteor. Atmos. Phys.,* **54,** 53–78.

——, J. Lamm, R. Adler, J. Alishouse, K. Aonashi, E. Barrett, P. Bauer, W. Berg, A. Chang, R. Ferraro, J. Ferriday, S. Goodman, N. Grody, C. Kidd, C. Kummerow, G. Liu, F. Marzano, A. Mugnai, W. Olson, G. Petty, A. Shibata, R. Spencer, F. Wentz, and T. Wilheit, 1998: Results of WetNet PIP-2 Project. *J. Atmos. Sci.,* **55,** 1483–1536.

WCRP, 1995: Report of the eighth session of the WCRP/GEWEX working group on data management for the Global Precipitation Climatology Project (GPCP), 28–30 September 1994, Offenbach, Germany. World Meteorological Organization, 21 pp. [Available from World Climate Research Programme, C. P. 2300, CH-1211 Geneva 2, Switzerland.]

Weng, F., R. R. Ferraro, and N. C. Grody, 1994: Global precipitation estimations using Defense Meteorological Satellite Program F10 and F11 special sensor microwave imager data. *J. Geophys. Res.,* **99,** 14 493–14 502.

Wilheit, T., A. T. C. Chang, and L. S. Chiu, 1991: Retrieval of monthly rainfall indices from microwave radiometric measurements using probability distribution functions. *J. Atmos. Oceanic Technol.,* **8,** 118–136.

——, R. Adler, S. Avery, E. Barrett, P. Bauer, W. Berg, A. Chang, J. Ferriday, N. Grody, S. Goodman, C. Kidd, D. Kniveton, C. Kummerow, A. Mugnai, W. Olson, G. Petty, A. Shibata, E. Smith, and R. Spencer, 1994: Algorithms for the retrieval of rainfall from passive microwave measurements. *Remote Sens. Rev.,* **11,** 163–194.

Xie, P., and P. A. Arkin, 1995: An intercomparison of gauge observations and satellite estimates of monthly precipitation. *J. Appl. Meteor.,* **34,** 1143–1160.